Role of local short-scale correlations in the mechanism of negative magnetization

Malvika Tripathi,[1,*] T. Chatterji,[2] H. E. Fischer,[2] R. Raghunathan,[1] Supriyo Majumder,[1] R. J. Choudhary,[1,†] and D. M. Phase[1]
[1]*UGC-DAE Consortium for Scientific Research, Indore 452001, India*
[2]*Institut Laue-Langevin, 38042 Grenoble Cedex, France*

(Received 18 May 2018; revised manuscript received 4 December 2018; published 22 January 2019)

We elaborate here why the antiferromagnetically ordered $GdCrO_3$ responds in a diamagnetic way under certain conditions by monitoring the evolution of the microscopic global and local magnetic phases. Using high-energy (∼0.3 eV) neutrons, the magnetic ordering is shown to adopt three distinct magnetic phases at different temperatures: G_x^{Cr}, A_y^{Cr}, F_z^{Cr} below Néel temperature (171 K); $(F_x^{Cr}, C_y^{Cr}, G_z^{Cr}) \cdot (F_x^{Gd}, C_y^{Gd})$ below 7 K; and an intermediate phase for 7 K $\leqslant T \leqslant$ 20 K in the vicinity of the spin-reorientation phase transition. Although bulk magnetometry reveals a huge negative magnetization (NM) in terms of both magnitude and temperature range [$M_{-\max}$ (18 K) ∼ 35$M_{+\max}$ (161 K), $\Delta T \sim 110$ K in the presence of $\mu_0 H = 0.01$ T], the long-range magnetic structure and derived ordered moments are unable to explain the NM. Real-space analysis of the total (Bragg's + diffuse) scattering reveals significant magnetic correlations extending up to ∼9 Å. Accounting for these short-range correlations with a spin model reveals spin frustration in the $S = 3$ ground state, comprising competing first-, second-, and third next nearest neighboring interactions with values $J_1 = 2.3$ K, $J_2 = -1.66$ K and $J_3 = 2.19$ K in the presence of internal field, governs the observance of NM in $GdCrO_3$.

DOI: 10.1103/PhysRevB.99.014422

I. INTRODUCTION

Negative magnetization (NM) in the magnetically ordered systems endowing a net magnetization opposite with respect to the applied field, besides being a fascinating subject from a fundamental scientific point of view, has also been associated with a number of debates regarding the origin and reproducibility of this phenomenon [1–3]. Since the hypothetical prediction of this phenomenon by Néel [4], a wide range of observations of NM have been noted in a variety of systems, including ferrites, rare-earth garnets, intermetallic alloys, spin chain and layered compounds [5–9]. Depending on the class of materials, the origin of the NM is also diverse; possible reasons include compensation of the magnetic moments at nonidentical magnetic sites in ferrimagnets under the framework of molecular field theory [4,10,11], the imbalance of spin and orbital moments [12,13], competition of single-ion anisotropy with Dzyaloshinskii-Moriya coupling [2,14,15], and phase inhomogeneity caused by a very small number of defects [16,17]. The perovskite RBO_3 (R = rare earth, B = transition metal) family, for which the difference in magnetic ordering temperatures of R^{3+} and B^{3+} ionic sites is huge ($^BT_N - {}^RT_N \geqslant 100$ K), also represents an intriguing class of such materials. Several members of the rare-earth orthochromite $RCrO_3$, orthoferrite $RFeO_3$, and orthovanadate RVO_3 families are known to realize this situation, either in undoped form or in chemically substituted compositions [2,18–21]. As the R^{3+} ions are paramagnetic in the observed NM regime, this class does not directly belong to Néel's oppositely coupled ferrimagnetic materials. In this case, the origin of NM is phenomenologically described by the assumption that the paramagnetic R^{3+} site is polarized by the internal magnetic field H_e imposed by the magnetically ordered B^{3+} ions, and the two nonequivalent magnetic species R^{3+} and B^{3+} (Cr, Fe, V) are coupled antiferromagnetically [22–26]. In the present work, we aim to revisit this hypothesis and understanding the origin of NM in the distorted orthorhombic perovskite $GdCrO_3$. The reasons justifying this choice include a huge magnitude of observed NM and broad temperature span $\Delta T \sim 110$ K in the presence of applied magnetic field $\mu_0 H = 0.01$ T, whereas the maximum absolute NM is ∼35 times larger than the maximum positive moment obtained, providing an ideal scenario for switching equipment. In addition, the observation of NM in $GdCrO_3$ also reveals the interesting dependency on the choice of measuring route, manifesting different behaviors in cooling and warming cycles. The phenomenological assumption comprising the opposite alignment of polarized paramagnetic Gd^{3+} ions with respect to Cr^{3+} ions is insufficient to explain the observed measuring path dependency of the NM.

The key reason for the discrepancy is the lack of understanding of the microscopic magnetic structure and its transformation with respect to the temperature. The presence of the very high neutron absorbing natural Gd element has been the reason so far to disregard the neutron diffraction measurements. High neutron absorption is a consequence of nuclear resonances of two Gd isotopes present in natural Gd: ^{155}Gd and ^{157}Gd at very low energies, $E = 0.0281$ eV and $E = 0.0312$ eV, respectively, whereas the resonance energy width is $\Delta E = 0.105$ eV [27]. To overcome the high absorption, we recorded the neutron diffraction profiles with incident neutron energy tuned to $E = 0.328$ eV ($\lambda = 0.4994$ Å), a value much higher than the resonance energy width. In the present study, we aim to construct the temperature-driven microscopic phase

*malvika@csr.res.in
†ram@csr.res.in

TABLE I. Structure parameters and reliability indicators obtained from Rietveld refinement of powder XRD at 300 K and neutron powder diffraction data at 300 and 3 K. Site occupancy is not considered as a variable during the refinement process.

	PXRD (300 K)	NPD (300 K)	NPD (3 K)
Lattice parameters (Å)	$a = 5.3170(2)$, $b = 5.5204(2)$, $c = 7.6084(3)$	$a = 5.3152(4)$, $b = 5.5204(5)$, $c = 7.6068(7)$	$a = 5.3157(9)$, $b = 5.5147(11)$, $c = 7.6009(8)$
Fractional coordinates			
Gd (4*c*)			
x	−0.00579(14)	−0.00698(51)	−0.00718(56)
y	0.05720(21)	0.05872(28)	0.06021(42)
z	0.25000	0.25000	0.25000
Cr (4*b*)			
x	0.50000	0.50000	0.50000
y	0.00000	0.00000	0.00000
z	0.00000	0.00000	0.00000
O1 (4*c*)			
x	0.09141(18)	0.09393(29)	0.09266(71)
y	0.46475(23)	0.4043(38)	0.40355(39)
z	0.25000	0.25000	0.25000
O2 (8*d*)			
x	−0.29334(41)	−0.30039(22)	−0.29892(37)
y	0.30384(29)	0.29831(68)	0.29451(79)
z	0.05749(18)	0.05608(35)	0.05167 (29)
Isotropic thermal factors ($Å^2$)			
B_{Cr}	0.028(3)	0.062(4)	0.051(11)
B_{Gd}	0.031(18)	0.016(5)	0.009(6)
Statistical parameters	$R_p = 20.75$, $R_{wp} = 15.10$, $R_{\rm exp} = 12.38$, $\chi^2 = 1.48$, Bragg *R* factor = 8.4242, RF factor = 10.7931	$R_p = 3.31$, $R_{wp} = 3.64$, $R_{\rm exp} = 1.71$, $\chi^2 = 4.52$, Bragg *R* factor = 0.4743, RF factor = 0.3064	$R_p = 0.826$, $R_{wp} = 1.01$, $R_{\rm exp} = 0.54$, $\chi^2 = 3.46$, Bragg *R* factor = 0.359, RF factor = 0.189

diagram and qualitatively understand the mechanism of NM in $GdCrO_3$.

II. EXPERIMENTAL METHODOLOGY

Crystal structure, phase purity, and valence states of chromium ions are confirmed using x-ray diffraction (Bruker D2 PHASER Desktop Diffractometer, Cu $K\alpha$, $\lambda = 1.54$ Å) and x-ray photoemission spectroscopy (XPS) with an Al $K\alpha$ ($E = 1486.7$eV) laboratory source. The details of the sample preparation, crystallographic phase refinement with respect to the Rietveld-generated model pattern, and valence state confirmation by XPS analysis are discussed in the Supplemental Material (SM) [28] with the help of references therein [29,30]. Magnetometric measurements are performed using a commercial SQUID-VSM (MPMS-7 T, Quantum Design). Temperature-dependent magnetization M(T) is measured in the conventional zero-field-cooled (ZFC), field-cooled cooling (FCC), and field-cooled warming (FCW) protocols. Before each M(T) measurement, a standard diamagnetic sample (indium) is mounted, followed by switching the superconducting magnet into "reset" mode, which locally warms the superconducting electromagnet above critical temperature, and as a consequence, the effective trapped magnetic field can be nullified to a value $\leqslant 0.0001$ T. The magnetic moment of indium is measured in the presence of $\mu_0 H = 0.0002$ T at 10 K, and the sign and magnitude of the magnetic moment are used to ensure that the trapped magnetic field is positive. All the M(T) measurements are performed with 1 K/min sweep rate. Temperature-dependent neutron diffraction data were collected from a two-axis diffractometer at D4 (disordered materials diffractometer) at Institut Laue-Langevin (ILL) using a wavelength of 0.4994 Å obtained by reflection of a Cu(220) monochromator [31]. Although the idea of utilizing "hot neutrons" is remarkable for Gd-containing single crystals [32–34], so far any report based on powdered samples is not available in the literature. The high counting rate and low background of the D4 instrument [35] have enabled us to unambiguously determine the thermal evolution of magnetic structure. After calibration of the sample, the neutron diffraction intensity was normalized using a standard vanadium sample and corrected for background attenuation, multiple scattering, and inelasticity (Placzek) effects. For refinement of the crystal and magnetic structure, the FULLPROF software package was used, and BASIREPS [36] was used for generating the irreducible representations (IRs). As reported by Lynn and Seeger [27], we used a value of 9.5 fm for the coherent neutron scattering length of Gd at 0.4994 Å. An absorption correction of 0.6142 was used during the magnetic structure refinement procedure. For magnetic pair distribution function (mPDF) calculations, the incident λ is 0.4994 Å, which provides the maximum possible momentum transfer $Q_{\rm max} = 24.3$ Å^{-1}.

III. RESULTS AND DISCUSSIONS

The room-temperature crystal structure is determined by Neutron powder diffraction (NPD) and powder X-ray

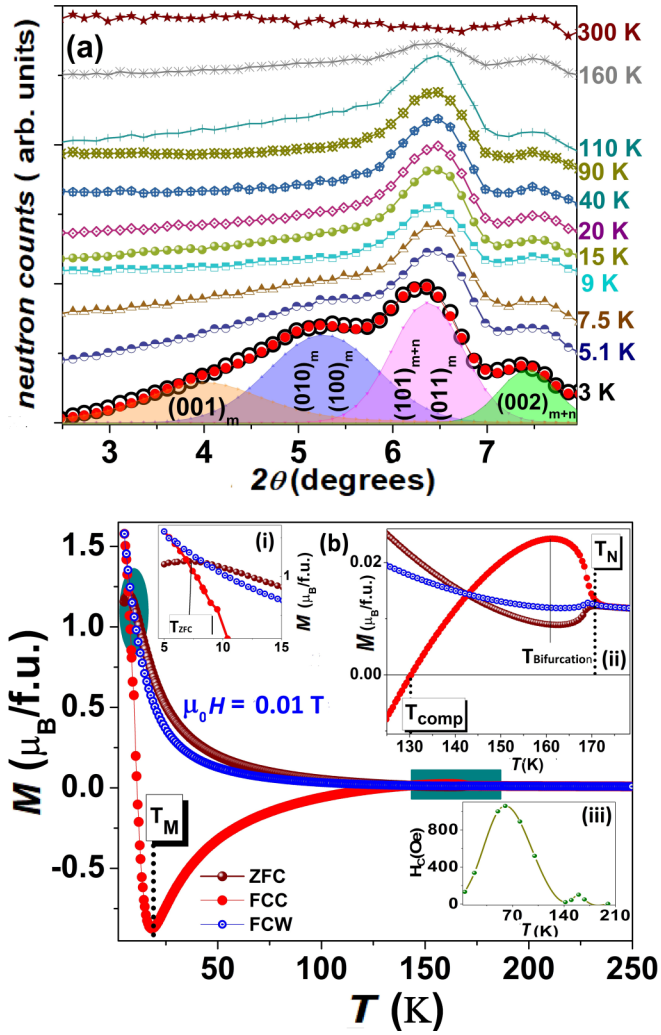

FIG. 1. (a) Thermal evolution of NPD patterns. (b) M(T) curves in ZFC, FCC, and FCW modes with measuring field $\mu_0 H = 0.01$ T. Insets (i) and (ii) show the variation of magnetization curves across $T_{\rm ZFC}$ and $T_{\rm comp}$ in an enlarged version. Inset (iii) shows nonmonotonic variation of coercivity with respect to temperature, indicating the temperature-dependent evolution of magnetic phases.

diffraction (PXRD) patterns presented in the SM [28]. The experimental data are refined with the help of calculated patterns generated by the *Pbnm* space group (D_{2h}^{16}, No. 62) and lattice parameters $\sqrt{2}a_p, \sqrt{2}a_p, 2a_p$, where a_p is the corresponding pseudocubic lattice parameter. The average values of a_p are 3.8221(5) and 3.8246(2) Å, obtained from refinement of NPD and PXRD data, respectively. The refined values of unit cell lengths, atomic positions, thermal coefficients, and reliability indicator factors are listed in Table I. The good agreement between the NPD and PXRD refined parameters indicates the reliability of neutron scattering measurements.

Figure 1(a) shows the thermal evolution of NPD patterns. Below 160 K, magnetic intensity emerges at the 2θ values corresponding to $(101)_{m+n}$ and $(011)_m$ Bragg's reflections. Below 20 K, the slight appearance of the $(010)_m + (100)_m$ doublet and $(001)_m$ can be observed, which becomes clearly visible below 7 K. It should be noted that the (011), (010)/(100), and (001) reflections are prohibited in the *Pbnm* space group, and hence, the intensity corresponding to these Bragg's planes appears only due to magnetic scattering.

Temperature-dependent magnetization curves measured in the ZFC, FCC, and FCW protocols in the presence of $\mu_0 H = 0.01$ T are shown in Fig. 1(b). The interplay of various exchange interactions between the three magnetic pairs Cr^{3+}-Cr^{3+}, Cr^{3+}-Gd^{3+}, and Gd^{3+}-Gd^{3+} leads to a number of observed temperature-driven magnetic orderings, which are nomenclatured as follows: (i) $T_N = 171$ K, attributed to the ordering of chromium sub-lattices in the canted antiferromagnetic structure, (ii) $T_{\rm bifurcation} = 160$ K, assigned with the change in the sign of the slope of the three magnetization curves (FCC moments start to drop, whereas FCW and ZFC moments tend to increase), (iii) $T_{\rm comp} = 130$ K, at which the net magnetic moment becomes fully compensated in the FCC mode, (iv) $T_M = 20$ K, attributed to the sharp change in moment values, and (v) $T_{\rm ZFC} = 7$ K, assigned to the change in slope of the magnetization curve in only the ZFC cycle. The temperature-dependent magnetic ordering process was described by Cooke *et al.* [37] on the basis of multiple exchange interactions. The Cr^{3+} ions order in a canted antiferromagnetic configuration below T_N, which is attributed to Dzyaloshinskii-Moriya exchange interactions [38,39]. The canted configuration of chromium magnetic moments induces an internal magnetic field H_e at each Gd site. The total magnetic moment is assumed to be the superposition of uncompensated moments at chromium sites M_{Cr} and the paramagnetic gadolinium magnetic moment M_{Gd} polarized due to H_e in the presence of applied magnetic field H_a, given as

$$M = M_{Cr} + M_{Gd} = M_{Cr} + C(H_a + H_e)/(T - \theta). \quad (1)$$

Using the magnetometric results, H_e was estimated to be -0.55 T, where the negative sign indicates the antiferromagnetic coupling of Cr^{3+} and Gd^{3+} sublattices [37]. Yoshii [26] recognized the consequence of the antiparallel alignment of Cr^{3+} and Gd^{3+} magnetic moments in the observance of NM realized in the FCC mode. The observed NM was remarkably stable with respect to time span as the magnetization measured at 30 K after field cooling in the presence of 0.01 T applied field revealed a variation of ~0.5% only on measuring after 2 days. The FCC magnetization was fitted using Eq. (1) with a value of $H_e = -0.15$ T.

Interestingly, as shown in Fig. 1(a), NM is observed only in the FCC cycle, indicating the dependence of magnetization on the path or history in a particular measurement. To account for the distinct susceptibility curves observed in the FCC and FCW cycles, Yoshii [40] assumed different values of H_e, opposite in sign but only slightly different in magnitude to empirically match the observed magnetic susceptibility. This model undoubtedly provides a significant match with the experimental data, but from a fundamental point of view, it is difficult to understand how the internal magnetic field switches its sign by changing only the measuring path. Moreover, Zhao *et al.* [21] and Bellaiche *et al.* [41] revealed that the effective magnetic field at rare-earth sites in RBO_3 materials (B = Cr, Fe) is governed by the microscopic coupling of antiferromagnetic (AFM) ordering of the B site magnetic

moment and oxygen octahedral tilting. The induced magnetic moment at the R site can be parallel or antiparallel with respect to the B site sublattice depending on the coupling constants, which have a characteristic value for a particular material. Therefore, it is difficult to understand why the sign of H_e of the chromium sublattice on the Gd site depends on the measuring route and consequently gives rise to the opposite alignment of Gd^{3+} ions with respect to Cr^{3+} ions.

In the $RCrO_3$ family, the crystallographic and magnetic unit cells are identical; that is, magnetic structure can be generated by the $\mathbf{k} = \mathbf{0}$ propagation vector. Chromium atoms are at 4*b* Wyckoff positions, and the atomic coordinates of these atoms are $(\frac{1}{2}, 0, 0)$, $(\frac{1}{2}, 0, \frac{1}{2})$, $(0, \frac{1}{2}, \frac{1}{2})$, and $(0, \frac{1}{2}, 0)$. Gadolinium atoms are at the 4*c* sites with atomic positions given as $(x, y, \frac{1}{4})$, $(-x, -y, \frac{3}{4})$, $(\frac{1}{2} + x, \frac{1}{2} - y, \frac{3}{4})$, and $(\frac{1}{2} - x, \frac{1}{2} + y, \frac{1}{4})$. For the *Pbnm* space group, the independent symmetry elements are two twofold screw axes, $\tilde{2}_x$ and $\tilde{2}_y$, at $(x, \frac{1}{4}, 0)$ and $(\frac{1}{4}, y, \frac{1}{4})$, respectively, and the inversion center $\bar{1}$ at the point (0,0,0). It should be noted that $\tilde{2}_z = \tilde{2}_x \cdot \tilde{2}_y$ and henceforth is not considered an independent symmetry element. For the sake of convenience, the linear combinations of spin vectors S_j (j = 1–4) which transform into themselves under the operation of symmetry elements defined as

$$F = S_1 + S_2 + S_3 + S_4,$$
$$A = S_1 - S_2 - S_3 + S_4,$$
$$C = S_1 + S_2 - S_3 - S_4,$$
$$G = S_1 - S_2 + S_3 - S_4,$$

form the basis vectors [42,43]. The definite transformation properties are called a representation. The representation analysis studied by Bertaut [42] helps us to assign the IRs of the space group to a known magnetic structure. The four allowed combinations for chromium 4*b* sites, denoted as Γ_i (i = 1, 2, 3, and 4), along with the BASIREPS-generated IRs and corresponding basis vectors are listed in Table II. In the case of Gd (4*c*) sites, there is a total of eight irreducible representations, comprising the additional four representations denoted as Γ_j (j = 5–8). The transformation properties of these representations and values of these components (moments) are also listed in Table II. The moments of chromium and gadolinium atoms are represented as (u, v, w) and (l, m, n), respectively. The reducible representation belonging to chromium 4*b* sites can be written as the linear combinations of irreducible matrices Γ_i:

$$3\Gamma_1 + 3\Gamma_2 + 3\Gamma_3 + 3\Gamma_4.$$

The magnetic structure is modeled with respect to the Rietveld-refined patterns using FULLPROF. It is observed that the magnetic structure below T_N can be generated with the $\mathbf{k} = 0$ propagation vector and Γ_4 or the G_x, A_y, F_z configuration, as shown in Fig. 2. The Γ_4 configuration is observed to be the most reliable magnetic structure for temperature values $20\,\mathrm{K} < T \leqslant T_N$. Below 20 K, no individual allowed IR is able to provide a reliable match to the experimental data, so we have generated the patterns with intermediate phases formed by possible combinations of two IRs. It may be argued that the inclusion of an additional phase and henceforth providing more degrees of freedom should improve the quality of

TABLE II. Character table generated for the *Pbnm* space group with $\mathbf{k} = \mathbf{0}$

IR	Symmetry elements			Spin modes		Magnetic moments at atomic positions							
	$\tilde{2}_x$	$\tilde{2}_y$	$\bar{1}$	Cr (4*b*)	Gd (4*c*)	Cr_1	Cr_2	Cr_3	Cr_4	Gd_1	Gd_2	Gd_3	Gd_4
Γ_1/IR(1)	+	+	+	A_x, G_y, C_z	·, ·, C_z	(u, v, w)	$(-u, -v, w)$	$(-u, v, -w)$	$(u, -v, -w)$	$(0, 0, n)$	$(0, 0, n)$	$(0, 0, -n)$	$(0, 0, -n)$
Γ_2/IR(5)	+	−	+	F_x, C_y, G_z	F_x, C_y, ·	(u, v, w)	$(u, v, -w)$	$(u, -v, w)$	$(u, -v, -w)$	$(l, m, 0)$	$(l, m, 0)$	$(l, -m, 0)$	$(l, -m, 0)$
Γ_3/IR(7)	−	+	+	C_x, F_y, A_z	C_x, F_y, ·	(u, v, w)	$(u, v, -w)$	$(-u, v, -w)$	$(-u, v, w)$	$(l, m, 0)$	$(l, m, 0)$	$(-l, m, 0)$	$(-l, m, 0)$
Γ_4/IR(3)	−	−	+	G_x, A_y, F_z	·, ·, F_z	(u, v, w)	$(-u, -v, w)$	$(u, -v, w)$	$(-u, v, w)$	$(0, 0, n)$	$(0, 0, n)$	$(0, 0, n)$	$(0, 0, n)$
Γ_5/IR(2)	+	+	−		G_x, A_y, ·					$(l, m, 0)$	$(-l, -m, 0)$	$(l, -m, 0)$	$(-l, m, 0)$
Γ_6/IR(4)	−	−	−		A_x, G_y, ·					$(l, m, 0)$	$(-l, -m, 0)$	$(-l, m, 0)$	$(l, -m, 0)$
Γ_7/IR(6)	+	−	−		·, ·, A_z					$(0, 0, n)$	$(0, 0, -n)$	$(0, 0, -n)$	$(0, 0, n)$
Γ_8/IR(8)	−	+	−		·, ·, G_z					$(0, 0, n)$	$(0, 0, -n)$	$(0, 0, n)$	$(0, 0, -n)$

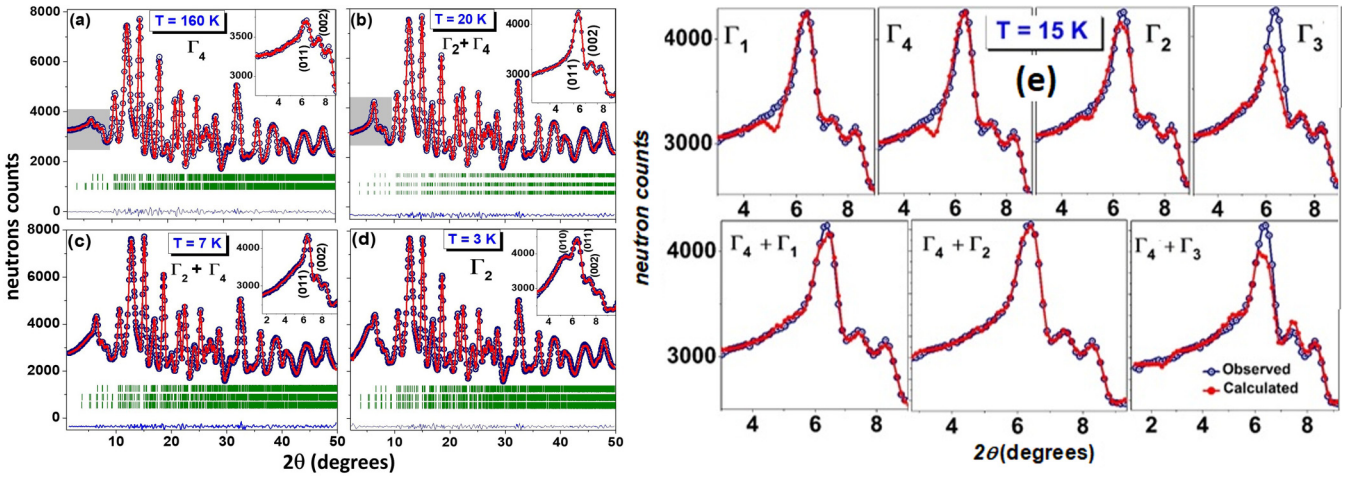

FIG. 2. (a)–(d) Neutron diffraction patterns along with Rietveld-generated calculated patterns at temperature values $T = 160$ K, $T = 20$ K, $T = 7$ K, and $T = 3$ K, respectively. Open circles and solid circles represent experimental and observed data points, respectively. Vertical bars denote Bragg's plane positions. Solid lines are a guide to the eyes. (e) Rietveld-generated patterns based on all possible magnetic configurations along with experimental pattern at $T = 15$ K.

the match anyhow. To justify the choice of the proper combination, we present the generated patterns with all individual IRs and their possible combinations, as shown in Fig. 2(e). It can be seen that $\Gamma_2 + \Gamma_4 \equiv \Gamma_{24}$ unambiguously provides the most reliable match with the experimental profile, and hence, it is assigned as the magnetic structure for $7\,\text{K} \leqslant T \leqslant 20\,\text{K}$, as shown in Figs. 2(b) and 2(c). Below 7 K, a clear enhancement in magnetic intensity is observed, corresponding to the $(010)_m + (100)_m$ doublet and $(001)_m$ Bragg's plane [Fig. 2(d)]. Based on the calculations of Shamir *et al.* [44], the appearance of the $(010)_m + (100)_m$ doublet is attributed to the ordering of Gd^{3+} moments. The magnetic structure below 7 K is generated with the ordering of chromium ionic sites (4*b*) in the Γ_2 (F_x, C_y, G_z) configuration along with Gd^{3+} (4*c*) ordering in the Γ_2 (F_x, C_y) configuration, as shown in Fig. 2(d). The spin arrangements in both Γ_2 and Γ_4 are illustrated in Figs. 3(a) and 3(b). In the Γ_4 (G_x, A_y, F_z) configuration, the magnetic moments of the nearest-neighbor Cr sites follow *G*-type ordering along the $x \parallel a$ direction, *A*-type ordering along $y \parallel b$, and ferromagnetic ordering along the $z \parallel c$ direction, resulting in an uncompensated weak moment along the *z* direction. Similarly, in the Γ_2 (F_x, C_y, G_z) configuration, the $x \parallel a$ components of magnetic moment order in the ferromagnetic configuration and henceforth the uncompensated moment is oriented along *x* crystallographic axis. In the temperature regime of $7\,\text{K} \leqslant T \leqslant 20\,\text{K}$, the direction of uncompensated spins reorients from the $z \parallel c$ axis (20 K) to the $x \parallel a$ axis (7 K), forming a spin-reorientation phase transition (SRPT). In the following, we shall denote the unidentified magnetic transitions T_M and T_{ZFC} as T_{SRPT} and T_{Gd}, respectively. It is noteworthy that no crystal or magnetic structural modification is observed across $T_{\text{bifurcation}}$ and T_{comp}; thus, we infer that the origin of magnetization reversal is not associated with magnetic phase transitions.

The variation of components of magnetic moment along different crystallographic directions obtained from Rietveld refinement is shown in Fig. 3(c). The component of the chromium magnetic moment along the *z* direction is very small in the Γ_4 phase, and the magnetic moment is mostly confined in the *a*-*b* plane only. The evolutions of magnetic moments along the *x* and *y* axes across $T_{\text{bifurcation}}$ and T_{comp} are almost opposite each other, indicating an in-plane rotation of magnetic moment from the $a \parallel x$ to $b \parallel y$ axis. All three moments reveal a significant drop in absolute moment value in the vicinity of T_{Gd}, and the moment values again start to become enhanced when the system is completely transformed into the Γ_2 phase below T_{Gd}, as shown in the insets of Fig. 3(c). The one-dimensional temperature-driven phase diagram along with variation of the total moment at chromium and gadolinium sites is shown in Fig. 3(d). The net magnetic moment of Gd^{3+} ionic sites is, however, sensitive to the temperatures T_{comp} and $T_{\text{bifurcation}}$; it is negative only for $T_{Gd} \leqslant T \leqslant 40\,\text{K}$ and not for the entire negative moment regime described by the bulk magnetization results. It reveals that the polarized magnetic moment of Gd does not make a significant contribution to the phenomenon of negative magnetization.

As the average long-range structure does not indicate NM, we aim to look for the nano-scale short-range correlations. We compute the real-space correlation functions and mPDFs by Fourier transformation of the total magnetic scattering intensity into real space, as shown in Fig. 4(a). The mPDF technique is sensitive to short-range correlations as the diffuse scattering is also accounted for in addition to Bragg's scattering [45,46]. Typically, a particular peak position in mPDF corresponds to a pair separation distance, the slope of the linear baseline depends on the spin orientation, the sign of the peak attributes the nature of ordering, and the peak height is a function of components aligned perpendicular to the connecting axis joining them. The contribution to the mPDF due to a pair of spins S_i and S_j separated by a distance r_{ij} is given as

$$f_{ij} = C\left[A_{ij}\delta(r - r_{ij})/r + B_{ij}\Theta(r_{ij} - r)r/r_{ij}^3\right],$$

where *C* is correlated to the spin quantum number, Θ is the Heaviside step function, and A_{ij} and B_{ij} are correlation coefficients determined by the alignment of the spins, generally positive for ferromagnetic-type alignment and

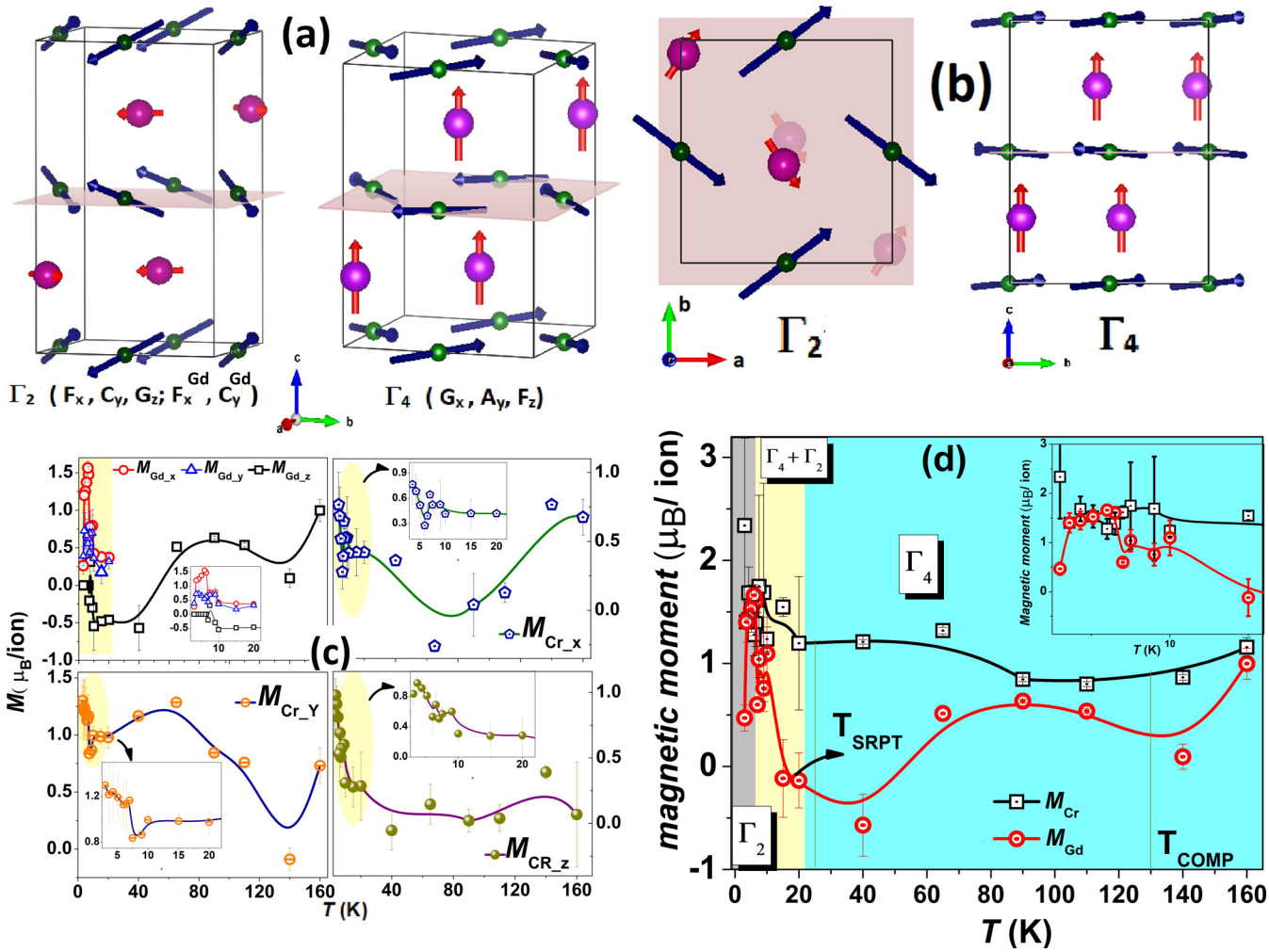

FIG. 3. (a) and (b) Illustrations of $\Gamma_4 \equiv G_x, A_y, F_z$ and $\Gamma_2 \equiv F_x, C_y, G_z$ magnetic spin configurations. (c) Variation of magnetic moment components along the x, y, and z directions. (d) Temperature-driven phase diagram of $GdCrO_3$ along with the variation of total Cr and Gd ionic moments with respect to temperature.

negative for antiferromagnetic arrangement [45]. To investigate the correlations between short-scale interactions and negative magnetization, we have calculated mPDF for difference diffraction patterns with reference to two baselines, one at 190 K, which is above the Néel temperature, and the second at 20 K (T_{SRPT}). The first two features (I and II) correspond to the exchange interactions between chromium-gadolinium first- and second-nearest-neighbor (NN and NNN) pairs, respectively. The third feature (III + IV + V), arising because of the convoluted effects of Gd-Gd NN, Cr-Cr NN, and Gd-Gd NNN interactions, is well defined and demonstrates resultant strong antiferromagnetic coupling. Similarly, the fourth feature (VI + VII), originating because of Cr-Cr NNN and Gd-Gd third-nearest-neighbor (NNNN) exchange interactions, is also prominent but indicates ferromagnetic ordering. The distinct peak VIII is attributed to the Cr-Gd NNNN interaction, which is ferromagnetic in nature, but its intensity is reduced as a factor of $1/r$. Features IX and X correspond to Cr-Cr NNNN and Gd-Cr fourth-nearest-neighbor (NNNNN) interactions, respectively. Peak XI represents the Gd-Gd NNNNN interactions. The corresponding atomic distances are illustrated in Fig. 4(c).

Analyzing the mPDF for two different types of spins is ambiguous, and hence, here, we will consider only the correlations in disordered Gd^{3+} spins. In the NM regime, there are significant local Gd^{3+}-Gd^{3+} three-dimensional antiferromagnetic interactions ranging up to the NNNNN distance, or ∼9 Å, even though the long-range structure of Gd is paramagnetic. The intensity of these Gd-Gd correlation peaks varies proportionally with the coordination number. Just below T_{SRPT}, when the magnetization flips to become positive in the FCC cycle, the intensity corresponding to the second- and third-nearest-neighbor interactions of Gd^{3+} drops. Noteworthily, the intensity attributed to Gd-Gd NNNNN interaction is now significantly reduced, whereas the feature belonging to the Gd NN interaction is enhanced, suggesting that the local Gd^{3+} correlations now cease.

To elucidate the nature of short-range correlations of Gd^{3+} ions, we have modeled the local interactions of Gd ions within the framework of the isotropic Heisenberg Hamiltonian. The model that we consider here involves the Gd sublattice in the presence of an effective magnetic field H_e^z, which is the sum of an externally applied field and the internal field due to the ordered Cr sublattice. The spin Hamiltonian describing the

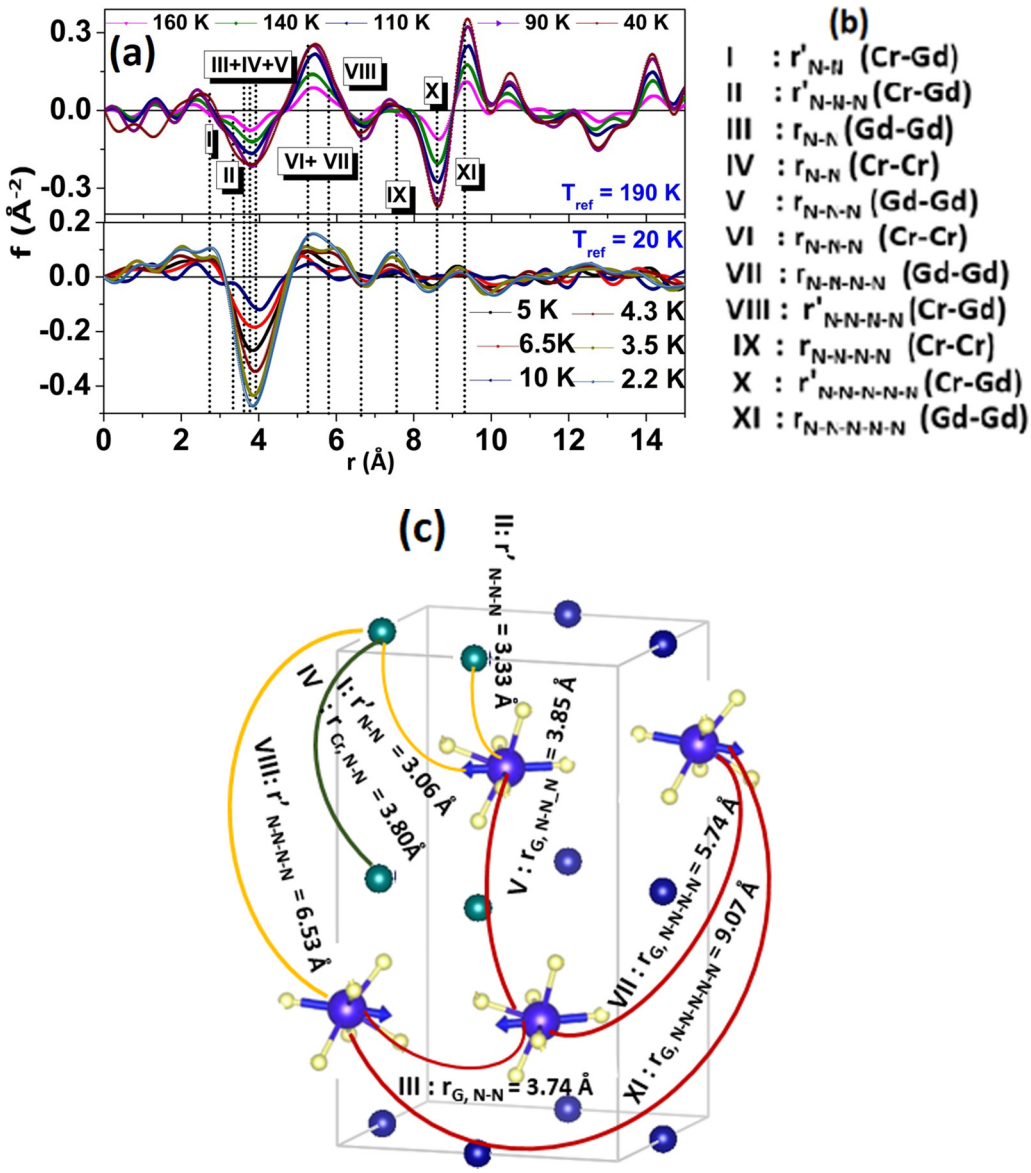

FIG. 4. (a) mPDF calculations with reference to two different base temperatures, $T = 190$ and 20 K. (b) List of various bond lengths, where r_{Cr}, r_{Gd}, and r' represent the Cr-Cr, Gd-Gd, and Cr-Gd bond lengths, respectively. (c) Illustration of various atomic distances in a single unit cell of $GdCrO_3$. Blue (large) and green (small) spheres represent Gd and Cr atoms, respectively. For the sake of clarity interatomic distances corresponding to VI [r_{N-N-N}(Cr-Cr)], IX [$r_{N-N-N-N-N}$(Cr-Cr)], and X ($r'_{N-N-N-N-N}$) are omitted.

system is given by

$$\hat{H} = -\sum_{i<j} J_{ij}\hat{\vec{s}}_i \cdot \hat{\vec{s}}_j - g\mu_B H_e^z \sum_i \hat{s}_i^z, \tag{2}$$

where the first and second terms in the equation correspond to Heisenberg exchange and Zeeman terms, respectively. In Eq. (2), J_{ij} is the magnetic exchange between sites i and j, $\hat{\vec{s}}_i$ are the site spin operators, g is the gyromagnetic ratio, taken to be 2.0, and μ_B is the Bohr magneton. Positive and negative values of J_{ij} correspond to ferromagnetic and antiferromagnetic interactions, respectively. As one can see from the Zeeman term, a positive value of magnetic field will stabilize the spin states with positive total M_s values. In the presence of negative effective magnetic field, spin states corresponding to negative magnetization are stabilized relative to those with positive magnetization, thus resulting in overall negative magnetization.

The magnetic exchange pathways within the unit cell of the system are shown in Fig. 5. From the unit cell topology, six Gd-Gd magnetic exchange pathways can be identified. Correspondingly, the model Hamiltonian can be written as

$$\begin{aligned}\hat{H} = &-J_{12}\hat{\vec{s}}_1 \cdot \hat{\vec{s}}_2 - J_{13}\hat{\vec{s}}_1 \cdot \hat{\vec{s}}_3 - J_{14}\hat{\vec{s}}_1 \cdot \hat{\vec{s}}_4 \\ &-J_{23}\hat{\vec{s}}_2 \cdot \hat{\vec{s}}_3 - J_{24}\hat{\vec{s}}_2 \cdot \hat{\vec{s}}_4 - J_{34}\hat{\vec{s}}_3 \cdot \hat{\vec{s}}_4 \end{aligned} \tag{3}$$

$$\begin{aligned}= &-J_1\hat{\vec{s}}_1 \cdot \hat{\vec{s}}_2 - J_2\hat{\vec{s}}_1 \cdot \hat{\vec{s}}_3 - J_4\hat{\vec{s}}_1 \cdot \hat{\vec{s}}_4 \\ &-J_3\hat{\vec{s}}_2 \cdot \hat{\vec{s}}_3 - J_2\hat{\vec{s}}_2 \cdot \hat{\vec{s}}_4 - J_1\hat{\vec{s}}_3 \cdot \hat{\vec{s}}_4. \end{aligned} \tag{4}$$

The sign and strength of various magnetic interactions in the unit cell can be ascertained from the Gd-O-Gd bond lengths d and angles θ, respectively, and they are presented

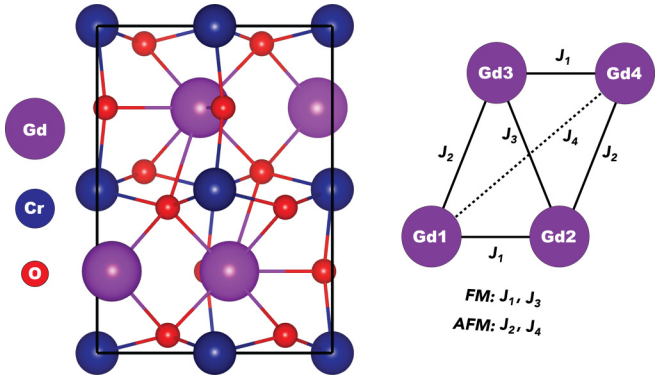

FIG. 5. Unit cell of $GdCrO_3$ (left) and pathways of magnetic exchange between Gd ions (right). J_i are the magnetic exchange strengths.

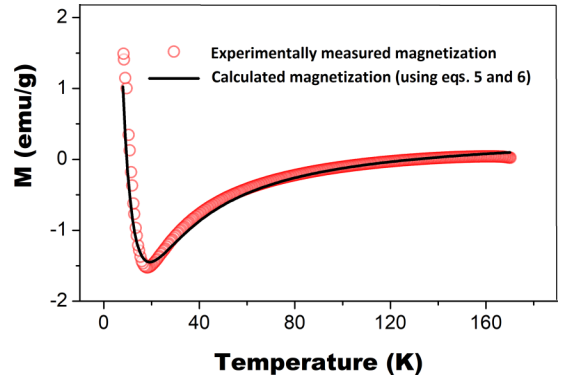

FIG. 6. Experimental magnetization data of $GdCrO_3$ and theoretical fit for $J_1 = 2.3\,\mathrm{K}$, $J_2 = -1.66\,\mathrm{K}$, $J_3 = 2.19\,\mathrm{K}$, and $J_4 = -0.23\,\mathrm{K}$; $H_e^z = -0.18\,\mathrm{T}$; and $D = 0.18\,\mathrm{K}$.

in Table III. The bond information suggests that there are only four unique magnetic exchange constants, J_1 through J_4, as shown in Eq. (4). Among these, the bond angles corresponding to J_1 and J_3 are approximately close to 90° and are expected to be ferromagnetic (FM; positive values of J). However, the bond angles for J_2 are closer to 180°, suggesting an antiferromagnetic interaction for this pathway. The exchange constant J_4 is taken to be weakly antiferromagnetic. A $1/d$ dependence can be assumed for the strength of magnetic interactions, and the magnitude of the strongest interaction is taken to be 1. Correspondingly, the starting values of exchange constants are fixed to $J_1 = 1.0$, $J_2 = -0.75$, $J_3 = 0.95$, and $J_4 = -0.47$. In the above equation, the Zeeman term is not included for the sake of simplicity. This term is diagonal as it involves only the z component of the spin operator, which will shift the energy eigenvalues by $-g\mu_B H_e^z M_S$, where M_S is the total magnetization of the eigenstate. This term is added separately to the energy eigenvalues while computing the magnetization.

The model Hamiltonian presented in Eq. (4) can be constructed in the basis of total spin S or the total z component of the total spin M_S, as the corresponding operators $\hat{S}^2$ and $\hat{S}^z$ commute with $\hat{H}$. In the present case, the H matrix is constructed in the constant M_S basis. Numerically solving the model Hamiltonian to obtain all the spin eigenstates $E(S, M_S)$ is discussed elsewhere [47]. Since the model Hamiltonian commutes with the $\hat{S}^2$ and $\hat{S}^z$ operators, the eigenstates of the Hamiltonian in Eq. (4) are also simultaneously the eigenstates of these operators. Hence, the total spin S and the total M_S of every eigenstate are obtained from the expectation values of the $\hat{S}^2$ and $\hat{S}^z$ operators. The canonical partition function is used to compute the magnetization arising from the Gd sublattice as a function of temperature T for a given value of effective magnetic field H_e^z:

$$M_{Gd}(T) = N_A g \mu_B \frac{\sum_S \sum_{M_S} M_S e^{-\frac{E_t(S,M_S)}{k_B T}}}{\sum_S \sum_{M_S} e^{-\frac{E_t(S,M_S)}{k_B T}}}. \quad (5)$$

In the above equation, the total energy of the eigenstate is given by $E_t(S, M_S) = E(S, M_S) - g\mu_B H_e^z M_S + D M_S^2$, and N_A is Avogadro's number. The additional terms in the energy expression are the Zeeman and anisotropy energies, respectively. The total magnetization of the system is given by

$$M(T) = M_{Cr}(T) + M_{Gd}(T) + M_P(T) + M_D, \quad (6)$$

where the terms on the right-hand side (RHS) of the equation are the magnetizations arising from the Cr sublattice, Gd sublattice, paramagnetic and diamagnetic impurity contributions, respectively. It should be noted that due to the very small canting angle the uncompensated magnetic moment of Cr^{3+} ions is very low in the Γ_4 configuration [48]. The estimated values of $M_{Cr}(T)$ range from $1.34(2) \times 10^{-3}$ to $9.22(7) \times 10^{-3}$ emu/g, which is orders of magnitude smaller than the total moment. Hence, for simplicity the magnetization contribution from the Cr sublattice can be neglected while fitting the total magnetization data. The third term in Eq. (6) corresponds to the magnetization due to free Gd spins and is of the form $C H_e^z / T$, where C is the Curie constant. As this term has $1/T$ dependence, the paramagnetic contribution is significant at very low temperatures.

The magnetization data are fitted iteratively by changing the relative strength of J_2, J_3, and J_4, keeping $J_1 = 1$. The fitted magnetization data are shown in Fig. 6. The best-fit parameters yield $J_1 = 2.3\,\mathrm{K}$, $J_2 = -1.66\,\mathrm{K}$, $J_3 = 2.19\,\mathrm{K}$, and $J_4 = -0.23\,\mathrm{K}$. The effective magnetic field used for the fit is $H_e^z = -0.17\,\mathrm{T}$, and the internal field due to the Cr sublattice on Gd ions is -0.18 T. The anisotropy constant used for the fit is $D = 0.18\,\mathrm{K}$. The ground state (GS) of the model in the absence of any magnetic field corresponds to a spin septet ($S_{GS} = 3$) due to the frustration induced by the exchange interaction. The energy spectrum of the model for $H_e^z = 0$, $H_e^z = -0.18\,\mathrm{T}$, and $H_e^z = -0.18\,\mathrm{T}$, $D = 0.18$ K is shown in Fig. 7. The low-lying spectrum of the model consists of very closely spaced excited states belonging to a

TABLE III. Gd-Gd distances, Gd-O-Gd bond angles, and the corresponding exchange type in the unit cell of $GdCrO_3$.

Ion pair	Distance (Å)	Bond angle (deg)	Exchange	Interaction
Gd1-Gd2	3.741(5)	84.13(7)°	J_1	FM
Gd1-Gd3	5.741(2)	177.30(3)°	J_2	AFM
Gd2-Gd3	3.861(6)	79.55(19)°	J_3	FM
Gd1-Gd4	8.905(5)		J_4	AFM

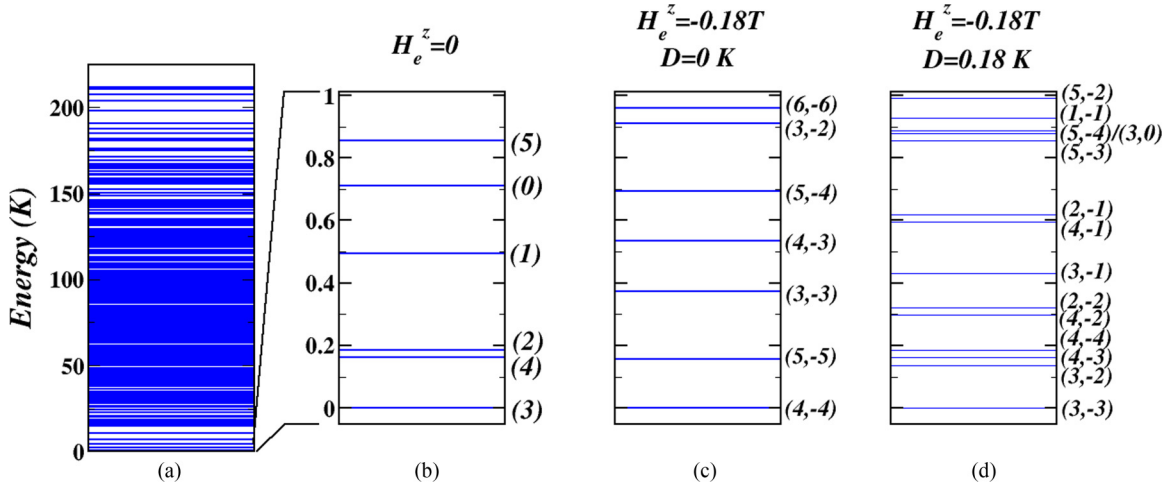

FIG. 7. (a) Calculated eigenspectrum of the model in Eq. (4) for $J_1 = 2.3$ K, $J_2 = -1.66$ K, $J_3 = 2.19$ K, and $J_4 = -0.23$ K. Zoom of the eigenspectrum in the energy range 0 to 1 K for (b) $H_e^z = 0$, (c) $H_e^z = -0.18$ T, and (d) $H_e^z = -0.18$ T, $D = 0.18$ K. In the $H_e^z = 0$ case, the spin states are $2S + 1$ degenerate and hence are indexed only by their total spin S^{tot}. For the $H_e^z = -0.18$ T cases, the degeneracy is lifted, and the states are indexed with $(S^{\text{tot}}, M_S^{\text{tot}})$.

total spin of 4, 2, 1, 0, and 5 within an energy gap of 1 K from the $S = 3$ GS. The excitation gaps are small due to the very weak exchange interactions present in the system. In the presence of negative magnetic field H_e^z, the $2S + 1$ degeneracy of the spin states is lifted. The states corresponding to the negative magnetization are stabilized relative to the positive ones, and $S^{\text{tot}} = 4$, $M_S^{\text{tot}} = -4$ becomes the ground state. The Boltzmann weights for these negative magnetization states are large at low temperatures, which leads to negative values of total magnetization. This situation is changed in the presence of the anisotropy term D, in which case the GS corresponds to $S^{\text{tot}} = 3$, $M_S^{\text{tot}} = -3$. This is because the positive nature of D destabilizes the states corresponding to both positive and negative magnetizations. This destabilization is greater for larger M_S values, and hence, $S^{\text{tot}} = 3$, $M_S^{\text{tot}} = -3$ stabilizes to the GS. Even in the presence of anisotropy, the low-lying states of the spectrum are completely dominated by states with negative M_S values. It should be noted that the paramagnetic contribution obtained from the fit is very large, with a Curie constant of $C = 70$ emu K/g. This signifies that at low temperatures the free-ion contribution to the total magnetization outweighs that of the correlated Gd spins, resulting in a crossover to positive magnetization. This large paramagnetic contribution can be corroborated with the very short range nature of magnetic correlations present in the system.

Our model thus provides insights into the complex nature and strength of magnetic exchange in the $GdCrO_3$ system. Although the presence of negative internal field created by the Cr sublattice leads to negative magnetization during the field-cooled cycle, our experimental findings show that the magnetization remains positive during the warming cycle. Here, we argue the possibility that the system with different initial population distributions in closely lying energy states and its distinct evolution with temperature lead to an entirely different path during the warming cycle. When the system is warmed gradually, the spins are excited from the GS spin manifold through a series of energy barriers. This is controlled by the internal conversion and intersystem crossings, as shown in Fig. 8. Internal conversion refers to excitation of spins within the same spin vector, whereas the intersystem crossings correspond to a crossover to a different total spin, obeying the spin selection rules ($\Delta S = \pm 1$). A purely paramagnetic state is achieved when the thermal energy is large enough to overcome the activation barriers to populate the high-lying states of the energy spectrum. Assuming that at absolute zero, all the spins are ordered and are stabilized in the $S^{\text{tot}} = 3$, $M_S^{\text{tot}} = -3$ GS, the warming cycle can be tracked by a set of kinetic rate equations which include internal conversions and intersystem crossings to various spin states [49]. In this case, the concentration of various spin species and hence the magnetization of the system depend on the solutions of the rate equations as a function of temperature and time. Such a model provides an understanding of the positive magnetization during the FCW cycle.

IV. CONCLUSIONS

In summary, we have constructed the temperature-driven magnetic phase diagram and discussed the origin of negative magnetization in $GdCrO_3$ by utilizing the high-energy $\lambda = 0.4994$ Å neutrons to overcome the huge absorption of natural Gd ions. Unambiguously, three distinct magnetic phase transformations were observed: chromium moments ordering in G_x, A_y, F_z with uncompensated moment along the $z \parallel c$ direction below Néel temperature $T_N = 171$ K; rotation of chromium weak ferromagnetic moments along the $x \parallel a$ crystallographic direction comprising the F_x, C_y, G_z spin configuration; and Gd moments ordering in the F_x, C_y configuration below $T_{Gd} = 7$ K. In the vicinity of the spin-reorientation phase transition ($7\text{ K} \leqslant T \leqslant 20\text{ K}$), an intermediate mixed-spin configuration is observed. Unexpectedly, no significant changes in long-range magnetic structure are observed across $T_{\text{compensation}}$ and $T_{\text{bifurcation}}$, suggesting that the NM is not associated with long-range magnetic phase transformations. Short-range Gd^{3+} correlation functions derived by mPDF calculations reveal the significant AFM correlations up to

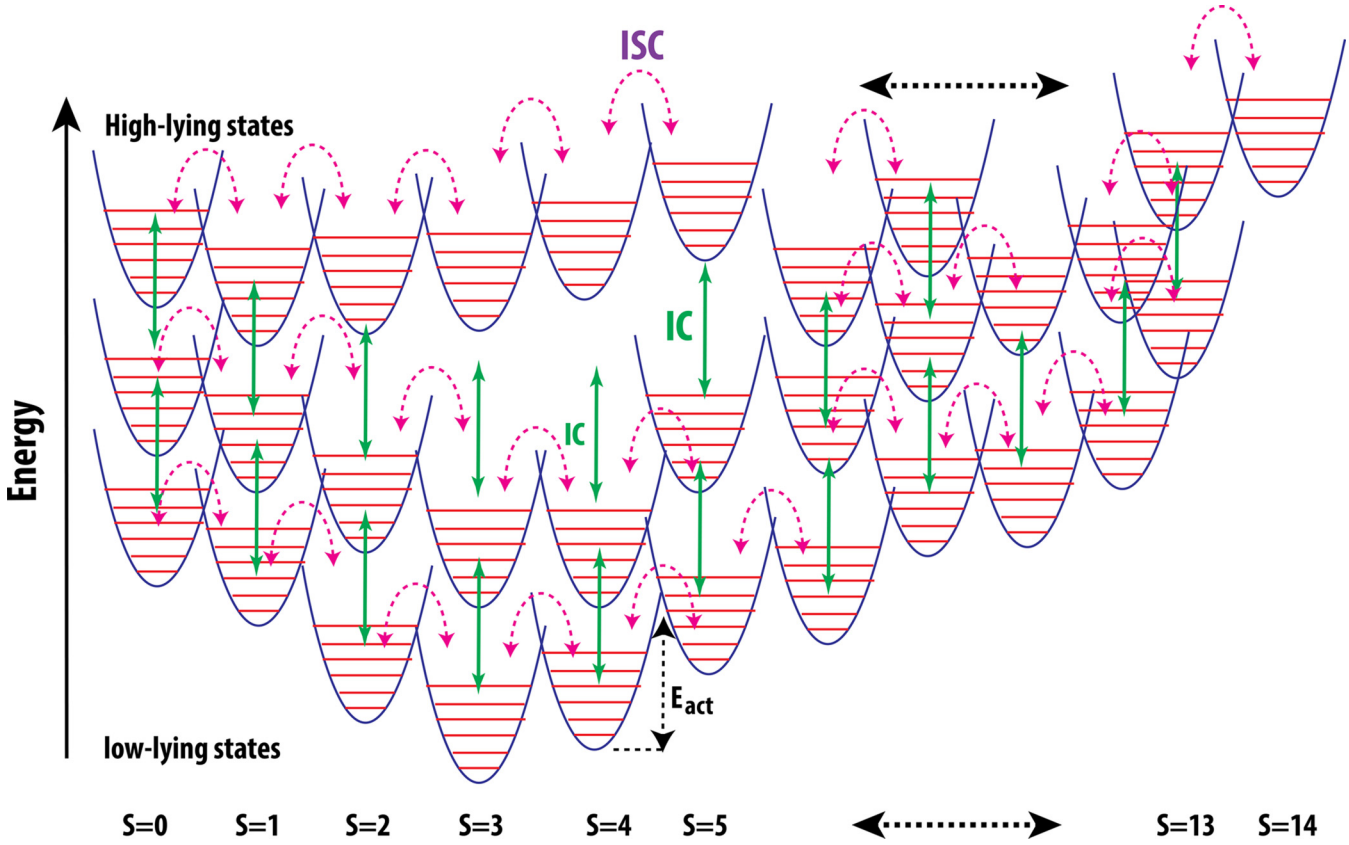

FIG. 8. Schematic of the kinetic process that involves internal conversion (IC) and intersystem crossings (ISC). The potential energy surface corresponding to various spin manifolds of the system is shown. Each spin manifold is connected to the other by an activation barrier E_{act}.

fourth-nearest-neighbor distance, or ∼9 Å, which cease below T_{SRPT}. Based on these observations, we have modeled the system with a model spin Hamiltonian. Results from our model calculations show that the exchange interactions between the Gd spins are extremely weak, leading to a set of closely spaced energy levels above the ground state. Competing exchange pathways in the system result in spin frustration, leading to a nonzero spin ground state. The presence of a negative effective magnetic field stabilizes the states with negative total M_S values. The path dependency in the observance of NM is understood as a consequence of the distinct population distribution in various closely spaced excited states with respect to cooling and warming paths.

ACKNOWLEDGMENTS

We are grateful to Dr. J. Rodriguez-Carvajal for reading the whole manuscript and providing salient comments. ILL, Grenoble, is thanked for providing access to the neutron diffraction facility.

[1] S. Gu, W. He, M. Zhang, T. Zhuang, Y. Jin, H. ElBidweihy, Y. Mao, J. H. Dickerson, M. J. Wagner, E. Della Torre *et al.*, Sci. Rep. **4**, 6267 (2014).
[2] Y. Ren, T. T. M. Palstra, D. I. Khomskii, E. Pellegrin, A. A. Nugroho, A. A. Menovsky, and G. A. Sawatzky, Nature (London) **396**, 441 (1998).
[3] A. A. Belik, Inorg. Chem. **52**, 8529 (2013).
[4] L. Neel, Ann. Phys. (Paris, Fr.) **12**, 137 (1948).
[5] N. Menyuk, K. Dwight, and D. Wickham, Phys. Rev. Lett. **4**, 119 (1960).
[6] Y. J. Hong, J. S. Kum, I.-B. Shim, and C. S. Kim, IEEE Trans. Magn. **40**, 2808 (2004).
[7] M. Hase, V. Y. Pomjakushin, V. Sikolenko, L. Keller, H. Luetkens, A. Dönni, and H. Kitazawa, Phys. Rev. B **84**, 104402 (2011).
[8] S. A. Chavan, R. Ganguly, V. K. Jain, and J. V. Yakhmi, J. Appl. Phys. **79**, 5260 (1996).
[9] K. H. J. Buschow, Phys. Status Solidi A **7**, 199 (1971).
[10] S. Chikazumi and C. D. Graham, *Physics of Ferromagnetism*, 2nd ed., International Series of Monographs of Physics, Vol. 94 (Oxford University Press, Oxford, 2009).
[11] J. S. Smart, Am. J. Phys. **23**, 356 (1955).
[12] H. Adachi and H. Ino, Nature (London) **401**, 148 (1999).
[13] H. Adachi, H. Kawata, H. Hashimoto, Y. Sato, I. Matsumoto, and Y. Tanaka, Phys. Rev. Lett. **87**, 127202 (2001).
[14] Y. Ren, T. T. M. Palstra, D. I. Khomskii, A. A. Nugroho, A. A. Menovsky, and G. A. Sawatzky, Phys. Rev. B **62**, 6577 (2000).
[15] H. C. Nguyen and J. B. Goodenough, J. Solid State Chem. **119**, 24 (1995).

[16] L. D. Tung, M. R. Lees, G. Balakrishnan, and D. McK. Paul, Phys. Rev. B **75**, 104404 (2007).
[17] L. D. Tung, Phys. Rev. B **73**, 024428 (2006).
[18] Y. Cao, S. Cao, W. Ren, Z. Feng, S. Yuan, B. Kang, B. Lu, and J. Zhang, Appl. Phys. Lett. **104**, 232405 (2014).
[19] M. P. Sharannia, S. De, R. Singh, A. Das, R. Nirmala, and P. Santhosh, J. Magn. Magn. Mater. **430**, 109 (2017).
[20] S. J. Yuan, W. Ren, F. Hong, Y. B. Wang, J. C. Zhang, L. Bellaiche, S. X. Cao, and G. Cao, Phys. Rev. B **87**, 184405 (2013).
[21] H. J. Zhao, J. Íñiguez, X. M. Chen, and L. Bellaiche, Phys. Rev. B **93**, 014417 (2016).
[22] Y. Su, J. Zhang, Z. Feng, L. Li, B. Li, Y. Zhou, Z. Chen, and S. Cao, J. Appl. Phys. **108**, 013905 (2010).
[23] K. Yoshii, Appl. Phys. Lett. **99**, 142501 (2011).
[24] J. Mao, Y. Sui, X. Zhang, Y. Su, X. Wang, Z. Liu, Y. Wang, R. Zhu, Y. Wang, W. Liu *et al.*, Appl. Phys. Lett. **98**, 192510 (2011).
[25] K. Yoshii and A. Nakamura, J. Solid State Chem. **155**, 447 (2000).
[26] K. Yoshii, J. Solid State Chem. **159**, 204 (2001).
[27] J. E. Lynn and P. A. Seeger, At. Data Nucl. Data Tables **44**, 191 (1990).
[28] See Supplemental Material at http://link.aps.org/supplemental/10.1103/PhysRevB.99.014422 for a description of the sample preparation method, XRD and NPD patterns at 300 K refined with respect to the Rietveld generated model pattern, and analysis of XPS for valence state determination .
[29] G. Allen and P. Tucker, Inorg. Chim. Acta **16**, 41 (1976).
[30] I. Ikemoto, K. Ishii, S. Kinoshita, H. Kuroda, M. A. Franco, and J. Thomas, J. Solid State Chem. **17**, 425 (1976).
[31] T. Chatterji and H. E. Fischer, Determining the magnetic configurations of $GdCrO_3$ using high energy neutrons, (Institut Laue-Langevin, 2017), doi: 10.5291/ILL-DATA.5-31-2516.
[32] T. Chatterji, A. Stunault, and P. J. Brown, Phys. Rev. B **97**, 064417 (2018).
[33] S. Bates, S. B. Palmer, J. B. Sousa, G. J. McIntyre, D. Fort, S. Legvold, B. J. Beaudry, and W. C. Koehler, Phys. Rev. Lett. **55**, 2968 (1985).
[34] G. Will, R. Nathans, and H. A. Alperin, J. Appl. Phys. **35**, 1045 (1964).
[35] H. E. Fischer, G. J. Cuello, P. Palleau, D. Feltin, A. C. Barnes, Y. S. Badyal, and J. M. Simonson, Appl. Phys. A: Mater. Sci. Process. **74**, s160 (2002).
[36] J. Rodríguez-Carvajal, Phys. B (Amsterdam, Neth.) **192**, 55 (1993).
[37] A. H. Cooke, D. M. Martin, and M. R. Wells, J. Phys. C **7**, 3133 (1974).
[38] I. Dzyaloshinsky, J. Phys. Chem. Solids **4**, 241 (1958).
[39] T. Moriya, Phys. Rev. **120**, 91 (1960).
[40] K. Yoshii, Mater. Res. Bull. **47**, 3243 (2012).
[41] L. Bellaiche, Z. Gui, and I. A. Kornev, J. Phys.: Condens. Matter **24**, 312201 (2012).
[42] E. F. Bertaut, Acta Crystallogr., Sect. A. **24**, 217 (1968).
[43] E. F. Bertaut, J. Appl. Phys. **33**, 1138 (1962).
[44] N. Shamir, H. Shaked, and S. Shtrikman, Phys. Rev. B **24**, 6642 (1981).
[45] B. Frandsen, X. Yang, and S. J. L. Billinge, Acta Crystallogr., Sect. A **70**, 3 (2014).
[46] B. A. Frandsen and S. J. L. Billinge, Acta Crystallogr., Sect. A **71**, 325 (2015).
[47] R. Raghunathan, S. Ramasesha, and D. Sen, Phys. Rev. B **78**, 104408 (2008).
[48] M. Tripathi, R. J. Choudhary, D. M. Phase, T. Chatterji, and H. E. Fischer, Phys. Rev. B **96**, 174421 (2017).
[49] R. Raghunathan, S. Ramasesha, C. Mathonière, and V. Marvaud, Phys. Chem. Chem. Phys. **10**, 5469 (2008).